Optimal illumination and wave form design for imaging in random media

Liliana Borcea
Computational and Applied Mathematics, MS 134, Rice University, 6100 Main Street, Houston, Texas 77005-1892

George Papanicolaou
Department of Mathematics, Stanford University, Stanford, California, 94305

Chrysoula Tsogka[a)]
Department of Applied Mathematics, University of Crete, Heraklion-Crete 71409, Greece

(Received 16 May 2007; revised 30 August 2007; accepted 22 September 2007)

The problem of optimal illumination for selective array imaging of small and not well separated scatterers in clutter is considered. The imaging algorithms introduced are based on the coherent interferometric (CINT) imaging functional, which can be viewed as a smoothed version of travel-time migration. The smoothing gives statistical stability to the image but it also causes blurring. The trade-off between statistical stability and blurring is optimized with an adaptive version of CINT. The algorithm for optimal illumination and for selective array imaging uses CINT. It is a constrained optimization problem that is based on the quality of the image obtained with adaptive CINT. The resulting optimal illuminations and selectivity improve the resolution of the images significantly, as can be seen in the numerical simulations presented in the paper.
© *2007 Acoustical Society of America.* [DOI: 10.1121/1.2799502]

PACS number(s): 43.60.Pt, 43.60.Gk, 43.60.Tj [PEB] Pages: 3507–3518

I. INTRODUCTION

We consider the imaging of small scatterers in cluttered media from the time traces of echoes recorded at a remote array. By clutter we mean inhomogeneities in the medium that are unknown and cannot be estimated in detail. In regimes with significant multiple scattering of the waves by the clutter, the time traces have considerable delay spread (coda) and their travel-time migration creates images with speckles that are difficult to interpret. The images are also unstable, which means that they change unpredictably with different realizations of the clutter.

To stabilize the imaging process in clutter, we introduced[1,2] the coherent interferometric (CINT) imaging functional. The images produced by CINT are statistically stable, that is, they have small variance with respect to random background fluctuations. Let us emphasize that it is the images that have small variance and not the background fluctuations, which have a sizable cumulative effect on wave propagation, and hence on the array data. CINT is a smoothed version of travel-time (Kirchhoff) migration[3,4] in which the delay spread is reduced by using the cross correlations of the traces over appropriate space-time windows,[1,5,6] rather than the traces themselves. The CINT images are then formed with travel-time migration of the local cross correlations. The choice of the space-time windows depends on the clutter and it affects both the statistical stability and the resolution of the image. We showed in Ref. 5 that there is a trade-off between these two effects, and we introduced an adaptive algorithm for selecting the size of the space-time windows so as to achieve an optimal compromise between gaining statistical stability and losing resolution by blurring.

In this paper we consider the imaging of a cluster of small scatterers that are close together and, because of the inevitable blur, cannot be distinguished with adaptive CINT. We introduce an algorithm for optimal illumination and selective imaging of the scatterers one at a time, in which we use the singular value decomposition (SVD) of the array response matrix, frequency by frequency.

The SVD of the response matrix has been used before[7–9] for obtaining optimal illuminations for detection of scatterers from the traces recorded at the array. These illuminations maximize the power of the signals recorded by the array. They are determined by the leading singular vector of the response matrix at the resonant frequency, which is where the leading singular value achieves its maximum over the bandwidth. However, the optimal illumination for detection is not appropriate for imaging because (1) the narrow bandwidth gives poor range resolution of the images and no statistical stability in clutter,[6,10,11] and (2) the leading singular vector does not necessarily illuminate a single (strongest) scatterer in the cluster. In general, this occurs only when the scatterers are well separated.

Well separated small scatterers can be imaged selectively in known media with the DORT method.[12] DORT stands for decomposition de l'opérateur de retournement temporel in French, which uses one singular vector at a time, over the entire bandwidth. However, DORT does not image selectively in clusters of nearby scatterers because the one-

[a)]Author to whom correspondence should be addressed. Electronic mail: tsogka@tem.uoc.gr

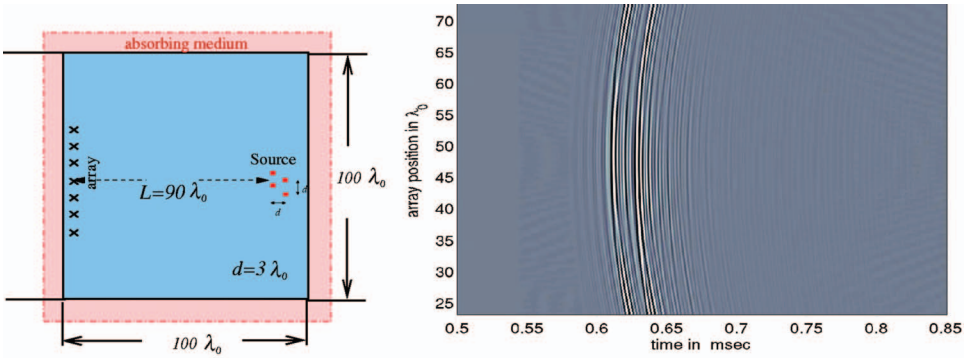

FIG. 1. Schematic of array imaging in a homogeneous medium. The computational setup is on the left. The traces received when illuminating from the central element in the array are on the right.

to-one correspondence between the scatterers and the singular vectors does not hold. It also does not give stable images when there is clutter.

There are three parts to the optimal illumination algorithm for selective imaging of clusters of small scatterers as presented in this paper. First, all imaging is based on the adaptive CINT functional, so that it is statistically stable in clutter. Second, the illumination is not done with one singular vector at a time, but with an optimal convex combination of the leading singular vectors across the bandwidth. The coefficients (subspace weights) are calculated by solving a constrained optimization problem which minimizes the support of the image, which is formed with adaptive CINT. Third, once the optimal subspace selection has been done so that the image is focused on a single scatterer, it is further improved by assigning optimal weights to each illuminating source in the array. These weights are also constrained minimizers of the support of the image.

The paper is organized as follows. In Sec. II we describe the setup for array imaging of a cluster of small scatterers. In Sec. III we describe the adaptive CINT algorithm and its relation to travel-time migration. In Sec. IV we consider the optimal illumination problem. We define the weighted subspaces using the SVD of the array response matrix in Sec. IV A, and then introduce the optimal illumination algorithm in Sec. IV B. We illustrate the performance of the algorithms with numerical simulations in the regime of ultrasonic array imaging in concrete.[13,14] Details and comments on the numerical results are given in Sec. V. We end with a summary and conclusions in Sec. VI.

II. PROBLEM SETUP

We consider imaging of a cluster of M small (point-like) scatterers at nearby locations $\mathbf{y}^{(j)}$ for $j=1,\ldots,M$, in a cluttered medium. The data are gathered with an array $\mathcal{A}$ of N_s sources and N_r receivers that is far from the scatterers. The sources are at points $\mathbf{x}_s \in \mathcal{A}$, for $s=1,\ldots,N_s$ and the receivers are at $\mathbf{x}_r \in \mathcal{A}$, for $r=1,\ldots,N_r$. The array illuminates the scatterers sequentially by sending a pulse $f(t)$ from the sources at $\mathbf{x}_s$ and recording for each pulse the traces $P(\mathbf{x}_r,\mathbf{x}_s,t)$ of the scattered echoes at the receivers

$$P(\mathbf{x}_r,\mathbf{x}_s,t) = f(t) \star \Pi(\mathbf{x}_r,\mathbf{x}_s,t) \tag{1}$$

for $r=1,\ldots,N_r$ and $s=1,\ldots,N_s$. Here $\Pi(t)=\{\Pi(\mathbf{x}_r,\mathbf{x}_s,t)\}$ is the $N_r \times N_s$ array impulse response matrix and the symbol $\star$ stands for time convolution. The traces $P(\mathbf{x}_r,\mathbf{x}_s,t)$ are recorded over a time window that is assumed for simplicity to be long enough (essentially infinite) so as to neglect it in Eq. (1). We also take for convenience the case of $N_s=N_r=N$ colocated sources and receivers. By reciprocity, this makes the array response matrix $\Pi(t)$ symmetric.

The probing pulse is of the form

$$f(t) = e^{-i\omega_0 t} f_B(t), \tag{2}$$

where ω_0 is the central frequency and $f_B(t)$ is the base-band pulse, with bandwidth B. In the frequency domain we have

$$\hat{f}(\omega) = \int_{-\infty}^{\infty} e^{i(\omega-\omega_0)t} f_B(t)dt$$

$$= \hat{f}_B(\omega-\omega_0) \neq 0 \quad \text{for } |\omega-\omega_0| \leqslant \frac{B}{2}, \tag{3}$$

where the symmetric interval of negative frequencies is suppressed for simplicity. We choose $\hat{f}_B(\omega)$ as the indicator function of the frequency interval $|\omega| \leqslant B/2$. This way, the Fourier coefficients of the traces coincide over the bandwidth with the Fourier coefficients of the response matrix

$$\hat{P}(\mathbf{x}_r,\mathbf{x}_s,\omega) = \hat{\Pi}(\mathbf{x}_r,\mathbf{x}_s,\omega) \tag{4}$$

for $s,r=1,\ldots,N$ and $|\omega-\omega_0| \leqslant B/2$.

A. Setup for the numerical simulation

The numerical simulations are in two dimensions, in a regime that is often used in ultrasonic array imaging in concrete.[13,14] In this paper, the elastic wave propagation in concrete is approximated by a scalar acoustic problem. Therefore, only pressure waves are considered and shear waves, Rayleigh waves, and mode conversion effects are neglected. We solve the acoustic wave equation as a first order velocity-pressure system with the finite element, time domain method given in Ref. 15, in two dimensions. The setup is shown in Figs. 1 and 2 for imaging in homogeneous and cluttered media, respectively. We simulate the wave propagation in an unbounded environment by surrounding the computational domain with a perfectly matched absorbing layer, as shown in Fig. 1.

The array is linear, with $N=100$ transducers at $\lambda_0/2$ apart and with an aperture $a=49.5\lambda_0$. We use the frequency band 150–450 kHz, with bandwidth $B=300$ kHz. The reference sound speed is $c_0=3$ km/s and therefore $\lambda_0=1$ cm. We have $M=4$ small scatterers at range $L=90\lambda_0$ from the array.

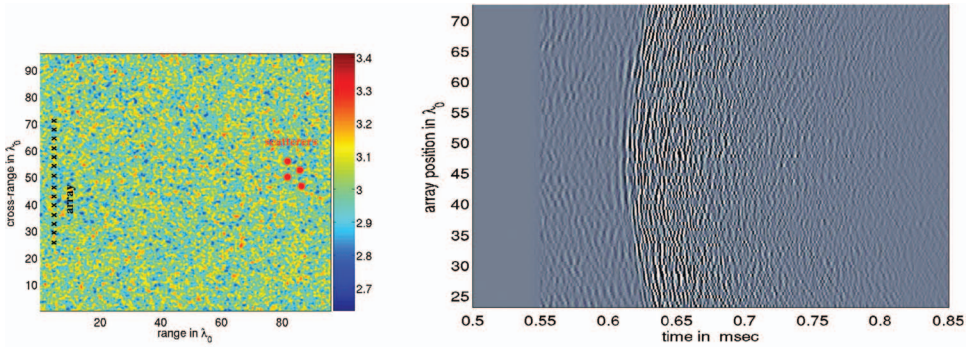

FIG. 2. Array imaging in clutter. The computational setup is shown on the left. The fluctuations in the sound speed are shown in color and the color bar is in km/s. The traces received when illuminating from the central element in the array are on the right.

They are at distance $d=3\lambda_0$ apart and we model them as soft acoustic disks of diameter λ_0, with the acoustic pressure equal to zero at their boundary. In concrete they correspond to air holes.

We model the clutter as a random process and write the square of the index of refraction $n(\mathbf{x})=c_0/c(\mathbf{x})$ in the form

$$n^2(\mathbf{x}) = n_0^2(\mathbf{x})\left[1+\sigma\nu\left(\frac{\mathbf{x}}{\ell}\right)\right]. \tag{5}$$

Here $n_0(\mathbf{x})$ is the smooth and known index of refraction of the background medium. We take $n_0(\mathbf{x})=1$ for simplicity, so that the wave speed $c(\mathbf{x})$ fluctuates about the constant value c_0. The normalized fluctuations are modeled by $\nu(\mathbf{x})$, which is a statistically homogeneous random process with mean zero and rapidly decaying correlation. The fluctuations have a characteristic length scale ℓ, the correlation length, for example, which can be considered to be the typical size of the inhomogeneities. The parameter σ controls the strength of the fluctuations.

The fluctuation process $\nu(\mathbf{x})$ is isotropic with Gaussian correlation

$$R(\mathbf{x},\mathbf{x}') = R(|\mathbf{x}-\mathbf{x}'|) = e^{-\frac{|\mathbf{x}-\mathbf{x}'|^2}{2\ell^2}}.$$

The correlation length is taken to be $\ell=\lambda_0/2$ and the fluctuation strength $\sigma=0.03$. Note that we are in a regime with small fluctuations $\sigma\ll 1$, as is expected in concrete structures. Nevertheless, because the range L is large with respect to λ_0 and ℓ, there is significant delay spread in the traces, as seen in Fig. 2. The estimated transport mean free path[16,17] in the clutter is $75\lambda_0$. This is to be contrasted with the time reversal experiments in Ref. 18, where the range is about ten transport mean free paths and all coherence is effectively lost in the echoes. Here the range L is comparable to the mean free path so there is some residual coherence in the data and coherent interferometric imaging can be effective.

III. ADAPTIVE COHERENT INTERFEROMETRIC IMAGING

In travel-time (Kirchhoff) migration the data traces are mapped to an image by the functional

$$\begin{aligned}\mathcal{I}^{\mathrm{KM}}(\mathbf{y}^S) &= \int_{|\omega-\omega_0|\le B/2} d\omega \sum_{r=1}^{N} e^{-i\omega\tau(\mathbf{x}_r,\mathbf{y}^S)} \\ &\quad\times \sum_{s=1}^{N} \hat{P}(\mathbf{x}_r,\mathbf{x}_s,\omega)e^{-i\omega\tau(\mathbf{x}_s,\mathbf{y}^S)} \\ &= \sum_{r=1}^{N}\sum_{s=1}^{N} P(\mathbf{x}_r,\mathbf{x}_s,\tau(\mathbf{x}_r,\mathbf{y}^S)+\tau(\mathbf{x}_s,\mathbf{y}^S)).\end{aligned} \tag{6}$$

Here $\mathbf{y}^S$ is a search point in the region where we form the image and $\tau(\mathbf{x}_r,\mathbf{y}^S)$ is the travel time of the waves from the array element $\mathbf{x}_r$ to $\mathbf{y}^S$, in the background medium with sound speed c_0. Since we assume a constant c_0,

$$\tau(\mathbf{x}_r,\mathbf{y}^S) = \frac{|\mathbf{x}_r-\mathbf{y}^S|}{c_0}.$$

In general but smooth media, τ is given by Fermat's principle.[19]

Travel-time migration of the traces when they have significant delay spread due to multiple scattering in clutter produces images with speckles that are difficult to interpret, as seen in the left picture of Fig. 3. The images are also unstable, in the sense that they change unpredictably with the realization of the clutter.

To stabilize the imaging process we introduced[1,2,6] the coherent interferometric (CINT) approach which migrates to $\mathbf{y}^S$ local cross correlations of the traces, computed over appropriately sized space-time windows. The CINT imaging function is

$$\begin{aligned}\mathcal{I}^{\mathrm{CINT}}(\mathbf{y}^S;\Omega_d,\kappa_d) &= \int_{|\omega-\omega_0|\le\frac{B}{2}} d\omega \int_{|\omega'-\omega_0|\le\frac{B}{2},|\omega-\omega'|\le\Omega_d} d\omega' \\ &\quad\times \sum_{r,r'\in\chi\left(\frac{\omega+\omega'}{2},\kappa_d\right)} \sum_{s,s'\in\chi\left(\frac{\omega+\omega'}{2},\kappa_d\right)} \\ &\quad\times \hat{Q}(\mathbf{x}_r,\mathbf{x}_s,\omega;\mathbf{y}^S)\overline{\hat{Q}(\mathbf{x}_{r'},\mathbf{x}_{s'},\omega';\mathbf{y}^S)},\end{aligned} \tag{7}$$

where the bar means complex conjugate and $\hat{Q}(\mathbf{x}_r,\mathbf{x}_s,\omega;\mathbf{y}^S)$ is the Fourier transform of the trace $P(\mathbf{x}_r,\ \mathbf{x}_s,t)$ migrated to $\mathbf{y}^S$

$$\hat{Q}(\mathbf{x}_r,\mathbf{x}_s,\omega;\mathbf{y}^S) = \hat{P}(\mathbf{x}_r,\mathbf{x}_s,\omega)e^{-i\omega[\tau(\mathbf{x}_s,\mathbf{y}^S)+\tau(\mathbf{x}_r,\mathbf{y}^S)]}. \tag{8}$$

Here the set of indices in the summation is defined by

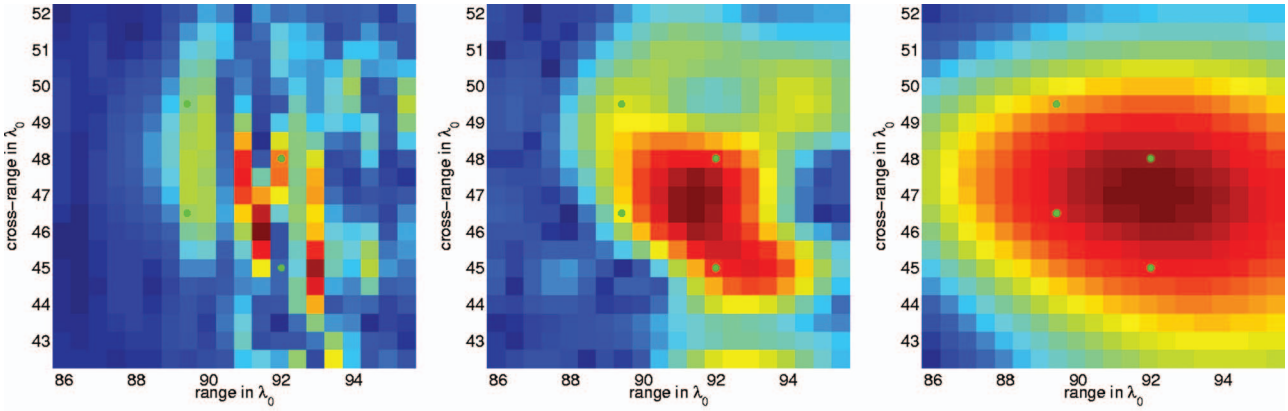

FIG. 3. The square root of the coherent interferometric imaging function for three choices of smoothing parameters. The left picture is with no smoothing, the middle picture is with optimal smoothing, and the right picture with too much smoothing. The four reflectors are indicated with green dots.

$$\chi(\omega,\kappa_d) = \left\{ r,r' = 1,\ldots,N; |\mathbf{x}_r - \mathbf{x}_{r'}| \leqslant X_d(\omega) = \frac{c_0}{\omega\kappa_d} \right\}. \tag{9}$$

The Ω_d and κ_d are clutter-dependent coherence parameters that must be estimated from the data. They determine the size of the time-space windows used to compute the local cross correlations of the traces, as we now explain.

The data appear in $\mathcal{I}^{\mathrm{CINT}}$ in the form $\hat{P}(\mathbf{x}_r,\mathbf{x}_s,\omega)\overline{\hat{P}(\mathbf{x}_{r'},\mathbf{x}_{s'},\omega')}$ for receiver and source location indexes in $\chi[(\omega+\omega')/2,\kappa_d]$, and for frequencies that are not more than Ω_d apart. This Ω_d is the decoherence frequency in clutter, defined as the smallest difference $|\omega-\omega'|$ over which $\hat{P}(\mathbf{x}_r,\mathbf{x}_s,\omega)$ and $\hat{P}(\mathbf{x}_r,\mathbf{x}_s,\omega')$ become statistically uncorrelated. When we restrict $|\omega-\omega'|\leqslant\Omega_d$ we have significant random phase cancellation in the local cross-correlation $\hat{P}(\mathbf{x}_r,\mathbf{x}_s,\omega)\overline{\hat{P}(\mathbf{x}_r,\mathbf{x}_s,\omega')}$. Equivalently, in the time domain, when we convolve $P(\mathbf{x}_r,\mathbf{x}_s,t)$ with its time reversed version over a time window of size $O(1/\Omega_d)$, we get a significant reduction of the delay spread.

The parameter κ_d defines the decoherence length $X_d(\omega)$, at frequency ω, as shown in Ref. 9. This decoherence length is the smallest separation between the sources $|\mathbf{x}_s-\mathbf{x}_{s'}|$ and between receivers $|\mathbf{x}_r-\mathbf{x}_{r'}|$ over which $\hat{P}(\mathbf{x}_r,\mathbf{x}_s,\omega)$ and $\hat{P}(\mathbf{x}_{r'},\mathbf{x}_{s'},\omega)$ become statistically uncorrelated. Thus, in CINT, we cross correlate the traces over space-time windows that are defined by the decoherence length and frequency in order to have significant reduction of the delay spread in the traces.

We showed[5,6] that thresholding of the space-frequency windows with X_d and Ω_d amounts to smoothing the image and giving it statistical stability. In very weak clutter, where there is little loss of coherence in the data, X_d and Ω_d can be as large as the aperture a and bandwidth B, respectively. Then $\mathcal{I}^{\mathrm{CINT}}$ becomes simply the square of $\mathcal{I}^{\mathrm{KM}}$. However, in stronger clutter X_d and Ω_d can be small compared to a and B, respectively, and then $\mathcal{I}^{\mathrm{CINT}}$ is a smoothed version of $|\mathcal{I}^{\mathrm{KM}}|^2$. The smoothing occurs by convolution with the window functions whose effective support is controlled by Ω_d and κ_d, as we explain in detail in Refs. 5 and 6. We showed[1,5] that the CINT point spread function has range resolution c_0/Ω_d and cross-range resolution $\lambda_0 L/X_d(\omega_0)=2\pi L\kappa_d$. These results should be compared with the Rayleigh resolution limits c_0/B and $\lambda_0 L/a$ for travel-time migration in homogeneous media.[19] For strong clutter, where $\Omega_d \ll B$ and $X_d(\omega_0)\ll a$, there is considerable loss of resolution.

The key question in the implementation of $\mathcal{I}^{\mathrm{CINT}}$ is how to estimate the clutter dependent parameters Ω_d and κ_d. This can be done directly from the data, using statistical techniques such as the variogram,[20] but it is a delicate process. We introduced[5] an adaptive version of the CINT algorithm that estimates Ω_d and κ_d during the image formation process by optimization of an objective function that quantifies the quality of the image.

CINT is a trade-off between smoothing for statistical stabilization and loss of resolution by blurring. This can be seen in Fig. 3, where we display the $\mathcal{I}^{\mathrm{CINT}}$ image computed with three different sets of parameters Ω_d and κ_d. On the left we show $\mathcal{I}^{\mathrm{KM}}$, which corresponds to setting $\Omega_d=B$ and $X_d=a$ across the bandwidth. On the right we show the square root of the oversmoothed image $\mathcal{I}^{\mathrm{CINT}}$, obtained with values for Ω_d and X_d that are too small. There are no speckles in this image. They have been removed by smoothing but we have also lost a lot of resolution. The middle picture in Fig. 3 shows the square root of $\mathcal{I}^{\mathrm{CINT}}$ for the optimal choice of Ω_d and X_d (i.e., κ_d) obtained by the following adaptive CINT algorithm.

Adaptive CINT algorithm: For given starting values of the parameters Ω_d and κ_d, calculate

$$\mathcal{J}(\mathbf{y}^S;\Omega_d,\kappa_d) = \frac{|\mathcal{I}^{\mathrm{CINT}}(\mathbf{y}^S;\Omega_d,\kappa_d)|^{1/2}}{\sup_{\mathbf{y}^S\in\mathcal{D}}|\mathcal{I}^{\mathrm{CINT}}(\mathbf{y}^S;\Omega_d,\kappa_d)|^{1/2}} \tag{10}$$

for $\mathbf{y}^S$ sweeping a search domain $\mathcal{D}$. For a suitably chosen parameter $\alpha>0$, estimate Ω_d and κ_d as the minimizers of

$$\mathcal{O}(\Omega_d,\kappa_d) = \|\mathcal{J}(\cdot;\Omega_d,\kappa_d)\|_{L^1(\mathcal{D})} + \alpha\|\nabla_{\mathbf{y}^S}\mathcal{J}(\cdot;\Omega_d,\kappa_d)\|_{L^1(\mathcal{D})}, \tag{11}$$

over all possible $\Omega_d\in[0,\ B]$ and $\kappa_d\geqslant 0$.

The first term in Eq. (11) favors images of small spatial support and the second term induces smoothing. This is essential for penalizing speckled images but the smoothing must be controlled in order to minimize the blurring. The

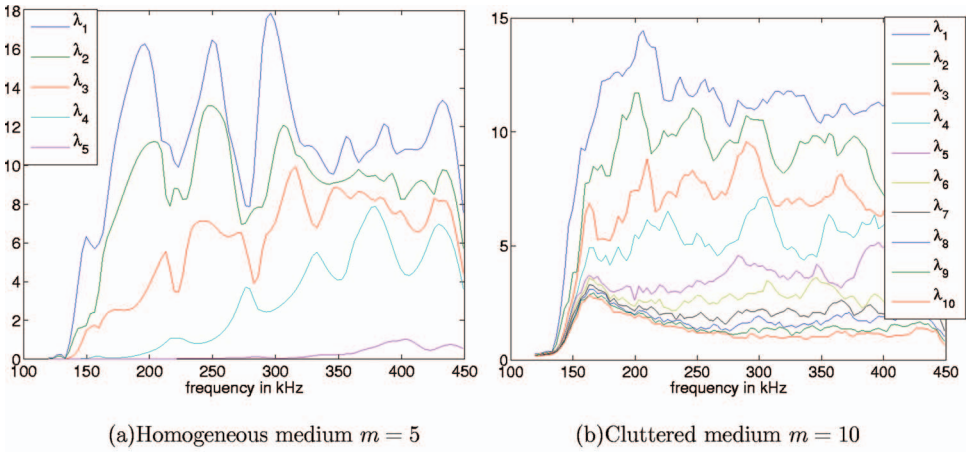

FIG. 4. The first m singular values of the response matrix as a function of frequency.

balance between the two terms in Eq. (11) is done with parameter $\alpha > 0$, which must be chosen in such a way that $\|\mathcal{J}(\cdot;\Omega_d,\kappa_d)\|_{L^1(\mathcal{D})}$ and $\alpha\|\nabla_{\mathbf{y}^S}\mathcal{J}(\cdot;\Omega_d,\kappa_d)\|_{L^1(\mathcal{D})}$ are of the same order. In principle, α can be changed during the estimation process. However, a good indication that the data respond well to the adaptive CINT algorithm is the relative stability of α as the iteration process for the determination of Ω_d and κ_d advances, until a plateau for the objective is reached. In all numerical simulations in this paper, and in previous ones,[5] $\alpha = 1$ worked well.

Note that in adaptive CINT we work with the square root of $|\mathcal{I}^{\mathrm{CINT}}|$. This is because we compare it with $\mathcal{I}^{\mathrm{KM}}$. When no smoothing is done then $|\mathcal{I}^{\mathrm{CINT}}|^{1/2}$ is equal to $|\mathcal{I}^{\mathrm{KM}}|$.

In the numerical setup considered in this paper (cf. Fig. 2) the scatterers are close together and, because of the inevitable blurring that CINT introduces, they cannot be distinguished with adaptive CINT. This is clear from the middle picture in Fig. 3. In order to image the scatterers separately, we introduce in the next section an algorithm for optimal illumination and selective imaging. In this algorithm we use the singular value decomposition (SVD) of the array response matrix, frequency by frequency. When the scatterers are not so closely spaced, or more precisely, when the blurring introduced is smaller than the distance in between the scatterers, then the adaptive CINT method can effectively distinguish them. Results for such a case are reported in Ref. 5.

IV. OPTIMAL ILLUMINATION AND SELECTIVE IMAGING WITH CINT

We introduce a two-step algorithm for optimal illumination and subspace selection with adaptive CINT in order to image clusters of small scatterers in clutter. The first step is described in Sec. IV A and it uses the singular value decomposition of the array response matrix to image the scatterers in a selective manner, one at a time. The second step is described in Sec. IV B. It is designed to improve the image of each scatterer using an optimal illumination from the array.

A. Selective imaging with CINT

1. Singular value decomposition of the response matrix

The singular value decomposition of the $N \times N$ response matrix $\hat{\Pi}(\omega) = \{\hat{\Pi}(\mathbf{x}_r, \mathbf{x}_s, \omega)\}$ at any frequency ω in the bandwidth is given by

$$\hat{\Pi}(\omega) = \sum_{j=1}^{N} \sigma_j(\omega)\hat{\mathbf{u}}_j(\omega)\hat{\mathbf{v}}_j^{\star}(\omega) \tag{12}$$

so that

$$\hat{\Pi}(\omega)\hat{\mathbf{v}}_j(\omega) = \sigma_j(\omega)\hat{\mathbf{u}}_j(\omega), \quad j = 1, \ldots, N. \tag{13}$$

Here the star stands for complex conjugate and transpose. The singular values $\sigma_j(\omega) \geqslant 0$ are in decreasing order and $\hat{\mathbf{u}}_j(\omega), \hat{\mathbf{v}}_j(\omega)$ are the orthonormal left and right singular vectors, respectively.

Because the complex matrix $\hat{\Pi}(\omega)$ is symmetric, although not Hermitian, we can determine the left singular vectors as the complex conjugates of the right ones. However, this is true only when the correct phase has been assigned to these vectors. The computation of the SVD with any public software returns

$$\hat{\mathbf{u}}_j(\omega) = e^{i\varphi_j(\omega)}\overline{\hat{\mathbf{v}}_j(\omega)}, \quad j = 1, \ldots, N \tag{14}$$

with an ambiguous phase that is difficult to unwrap in a consistent manner across the bandwidth. Nevertheless, the projection matrices

$$\mathcal{P}_j(\omega) = \hat{\mathbf{u}}_j(\omega)\hat{\mathbf{u}}_j^{\star}(\omega) \tag{15}$$

onto the space spanned by the jth left singular vector have no phase ambiguities, and this is what we use in the algorithm described below.

2. Data filtering

Let us assume that the number N of array elements is larger than the number M of small scatterers in the cluster. Then there are $n^{\star}(\omega) < N$ significant singular values of $\hat{\Pi}(\omega)$, with $n^{\star}(\omega) \sim M$. See Fig. 4 for an illustration of this fact, for the numerical setup described in Sec. II A, where $M = 4$. We note in Fig. 4(a) that in the homogeneous medium we can set

$n^\star(\omega)=4$. In the random medium Fig. 4(b) shows that we can set $n^\star(\omega)=5$ or at most 6, because for all indices beyond this threshold the singular values level off as when there is additive noise across the bandwidth. Note also that this threshold stays basically the same across the bandwidth, so we can write

$$n^\star(\omega) \approx n^\star(\omega_0). \tag{16}$$

This is because we are dealing with small, point-like scatterers. In the case of extended scatterers $n^\star(\omega)$ does vary across the bandwidth, as was shown before,[21] and this has to be taken into account when doing selective imaging of such reflectors.

Using the threshold $n^\star(\omega_0)$, we now define a set of filtering operators that we wish to apply to the data.

Definition 1 *Let Δ be the set of non-negative subspace weights*

$$\Delta = \{d_j(\omega) \geqslant 0 \text{ for } j = 1, \ldots, n^\star(\omega_0), \quad |\omega - \omega_0| \leqslant \frac{B}{2} \text{ and } \sum_{j=1}^{n^\star(\omega_0)} \int_{|\omega-\omega_0|\leqslant \frac{B}{2}} d_j(\omega) d\omega = 1\}.$$

We define the filtering operators $D(\omega,\cdot):\Delta \to \mathbb{C}^{N\times N}$, which take coefficients $d \in \Delta$ and return a linear combination of the projection matrices (15)

$$D(\omega,d) = \sum_{j=1}^{n^\star(\omega_0)} d_j(\omega)\mathcal{P}_j(\omega) \tag{17}$$

for each frequency ω in the bandwidth.

When we apply these filters to the response matrix, we get

$$D(\omega,d)\hat{\Pi}(\omega) = \sum_{j=1}^{n^\star(\omega_0)} d_j(\omega)\mathcal{P}_j(\omega)\hat{\Pi}(\omega) = \sum_{j=1}^{n^\star(\omega_0)} d_j(\omega)\sigma_j(\omega)\hat{\mathbf{u}}_j(\omega)\hat{\mathbf{u}}_j^T(\omega), \tag{18}$$

where we removed the null space of $\hat{\Pi}(\omega)$. Note that here the singular vectors $\hat{\mathbf{u}}_j(\omega)$ have the correct phase (i.e., $\varphi_j(\omega)=0$ in (14)). This correct phase is obtained by computing the projection $\mathcal{P}_j(\omega)\hat{\Pi}(\omega)$ of $\hat{\Pi}(\omega)$, which does not suffer from the phase ambiguity.

Now if we distinguish the subsets Δ_p of Δ, for $p=1,\ldots,n^\star(\omega_0)$,

$$\Delta_p = \{d \in \Delta;\ d_p(\omega) = \frac{1}{B} \text{ for } |\omega-\omega_0| \leqslant \frac{B}{2} \text{ and } d_j(\omega) = 0 \text{ for } j \neq p,\ j = 1, \ldots, n^\star(\omega_0)\},$$

we note that $D(\omega,d)$ for $d \in \Delta_p$ filters out the contribution of all singular vectors, except the pth one, uniformly across the bandwidth. This is what is done at the pth step of the basic DORT algorithm. The travel-time migration of the filtered data $D(\omega,d)\hat{\Pi}(\omega)$ gives the imaging function

$$\mathcal{I}(\mathbf{y}^S,p) = \int_{|\omega-\omega_0|\leqslant\frac{B}{2}} d\omega\sigma_p(\omega)\sum_{s=1}^{N}\sum_{r=1}^{N}\hat{u}_p(\mathbf{x}_s,\omega) \times \hat{u}_p(\mathbf{x}_r,\omega)e^{-i\omega[\tau(\mathbf{x}_s,\mathbf{y}^S)+\tau(\mathbf{x}_r,\mathbf{y}^S)]} = \int_{|\omega-\omega_0|\leqslant\frac{B}{2}} d\omega\sigma_p(\omega)\left[\sum_{s=1}^{N}\hat{u}_p(\mathbf{x}_s,\omega)e^{-i\omega\tau(\mathbf{x}_s,\mathbf{y}^S)}\right]^2. \tag{19}$$

We call this the DORT image because it uses one singular vector at a time. We recall that in the original DORT method,[12] the singular vectors are computed at each frequency and then a time-domain signal is formed from them and is backpropagated. To construct this signal in time, the phase of the singular vectors is used to compute the time delay that it needs at the array in order to focus. We can also describe DORT as an imaging method in which each singular vector over the bandwidth is backpropagated and the images are then summed over frequencies. The backpropagation is done in a homogeneous medium. In such a medium, DORT and iterative time reversal[22] are essentially equivalent and can be used either for detection or for imaging of small targets. In iterative time reversal the backpropagation step is done by *physically* transmitting the time reversed signal from the transducer array, repeatedly until it focuses on the strongest target. In a random medium iterative time reversal is an excellent *detection* method because it is not sensitive to the random inhomogeneities. This is another manifestation of statistical stability in time reversal.[6,10,11] The issue of iterative time reversal versus DORT as a *detection* method with noisy signals is also discussed in Chapter 10 of Ref. 23. Imaging in clutter is addressed[24,25] using the singular value decomposition and time correlation techniques. The algorithms based on adaptive CINT that are presented in this paper are, however, more flexible and effective.

Note that when we use just one source in Eq. (19) we get

$$\tilde{\mathcal{I}}(\mathbf{y}^S,p,\mathbf{x}_s) = \int_{|\omega-\omega_0|\leqslant\frac{B}{2}} d\omega\sigma_p(\omega)[\hat{u}_p(\mathbf{x}_s,\omega)e^{-i\omega\tau(\mathbf{x}_s,\mathbf{y}^S)}] \times \left[\sum_{r=1}^{N}\hat{u}_p(\mathbf{x}_r,\omega)e^{-i\omega\tau(\mathbf{x}_r,\mathbf{y}^S)}\right]. \tag{20}$$

When $p=1$ and $\sigma_p(\omega)$ is constant in the bandwidth, this can be interpreted as the image produced by travel-time migration of the traces obtained with the illumination produced by iterative time reversal[7,8] in echo mode. Indeed, suppose that we illuminate the scatterers from the source at $\mathbf{x}_s \in \mathcal{A}$ and we record the echoes

$$\hat{P}(\mathbf{x}_r,\mathbf{x}_s,\omega) = \hat{\Pi}(\mathbf{x}_r,\mathbf{x}_s,\omega), \quad r = 1, \ldots, N.$$

This is the s column of the response matrix written in short $\hat{\Pi}(\cdot,\mathbf{x}_s,\omega)$. Now, if we time reverse these signals and we reemit them in the medium, we get back the new vector

$$\hat{\Pi}(\omega)\overline{\hat{\Pi}(\cdot,\mathbf{x}_s,\omega)}.$$

Iterating this way, we converge to the leading singular vector as is well known.[7,8] However, this singular vector is com-

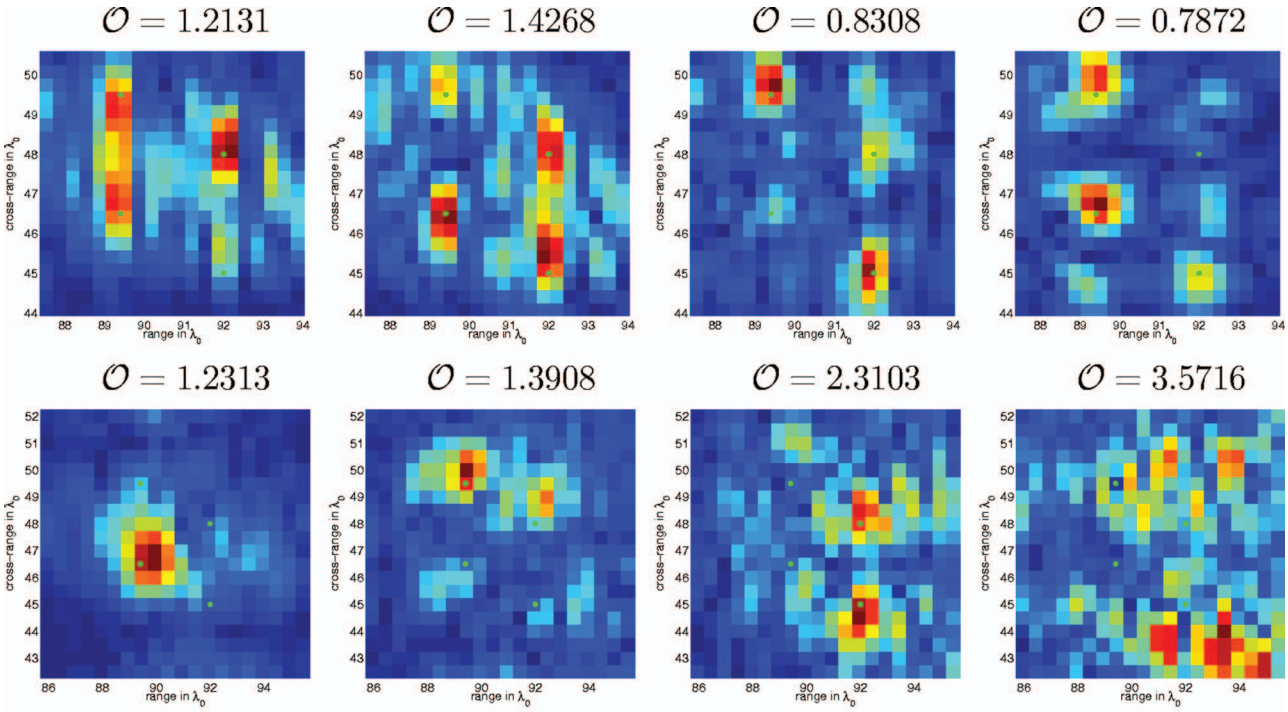

FIG. 5. DORT images using the first, second, third and fourth singular vector across the bandwidth. Top row: homogeneous medium. Bottom row: random medium. Above each plot we give the value of the L^2 norm of the image normalized by its maximum, which we denote by $\mathcal{O}$.

puted with the phase of $\hat{u}(\mathbf{x}_s,\omega)$ that is inherited from the original illumination from the source at $\mathbf{x}_s$. This phase is compensated in Eq. (20) with the travel time $\tau(\mathbf{x}_s,\mathbf{y}^S)$ to the search point $\mathbf{y}^S$ where the image peaks. The DORT images (20) peak on one scatterer at a time, if these are well separated, in the sense that the pth singular value is associated with the same scatterer uniformly in the bandwidth. However, in clusters of nearby scatterers DORT does not give selective images because the one-to-one correspondence between the singular values and the scatterers does not hold across the bandwidth. This is seen clearly in the plots of the top row of Fig. 5. Moreover, DORT does not give stable images in clutter as can be seen in plots of the bottom row of Fig. 5.

3. Selective imaging algorithm

To image the scatterers one by one, we formulate an iterative algorithm with two parts that we now describe.

Part 1: We estimate first the clutter-dependent decoherence parameters Ω_d and K_d using adaptive CINT. This estimation is done as described in Sec. III with the CINT imaging function (7) that uses the unfiltered array response matrix $\hat{\Pi}(\omega)$. The resulting image is shown in the middle in Fig. 3. The numerical setup is described in Sec. II A.

We note that we may also be able to estimate Ω_d and κ_d using CINT with array data coming from a known small scatterer, a pilot, whose range is comparable to that of the cluster that we wish to image selectively.

Part 2: With Ω_d and κ_d fixed, as found in Part 1, define the CINT image using the filtered data $D(\omega,d)\hat{\Pi}(\omega)$

$$\mathcal{I}^{\mathrm{CINT}}(\mathbf{y}^S;\Omega_d,\kappa_d;d) = \int_{|\omega-\omega_0|\leq\frac{B}{2}} d\omega \int_{|\omega'-\omega_0|\leq\frac{B}{2},|\omega-\omega'|\leq\Omega_d} d\omega' \times \sum_{r,r'\in\chi\left(\frac{\omega+\omega'}{2},\kappa_d\right)} \sum_{s,s'\in\chi\left(\frac{\omega+\omega'}{2},\kappa_d\right)} \times \hat{Q}_d(\mathbf{x}_r,\mathbf{x}_s,\omega;\mathbf{y}^S)\overline{\hat{Q}_d(\mathbf{x}_{r'},\mathbf{x}_{s'},\omega';\mathbf{y}^S)} \tag{21}$$

for arbitrary $d\in\Delta$. Here $\hat{Q}_d(\mathbf{x}_r,\mathbf{x}_s,\omega;\mathbf{y}^S)$ is the filtered data migrated to $\mathbf{y}^S$

$$\hat{Q}_d(\mathbf{x}_r,\mathbf{x}_s,\omega;\mathbf{y}^S) = [D(\omega,d)\hat{\Pi}(\omega)]_{r,s}e^{-i\omega[\tau(\mathbf{x}_s,\mathbf{y}^S)+\tau(x_r,\mathbf{y}^S)]} \tag{22}$$

and the set $\chi(\omega,\kappa_d)$ is defined in Eq. (9) in terms of κ_d. Now we begin the iteration:

Step 1: Find the optimal filter $D(\omega,d)$, for $|\omega-\omega_0|\leq B/2$, by minimizing the objective function

$$\mathcal{O}(d) = \|\mathcal{J}(\cdot\,;d)\|_{L^1(\mathcal{D})},$$

$$\mathcal{J}(\mathbf{y}^S;d) = \frac{|\mathcal{I}^{\mathrm{CINT}}(\mathbf{y}^S;\Omega_d,\kappa_d;d)|^{1/2}}{\sup_{\mathbf{y}^S\in\mathcal{D}}|\mathcal{I}^{\mathrm{CINT}}(\mathbf{y}^S;\Omega_d,\kappa_d;d)|^{1/2}} \tag{23}$$

over all subspace weights $d\in\Delta$. This optimization seeks images of small spatial support. There is no need to penalize the gradient here because all the statistical smoothing has been done by the thresholding with Ω_d and X_d (i.e., κ_d). The optimization involves $n^\star(\omega_0)N_\omega$ variables $d_j(\omega_m)$, for $j=1,\ldots,n^\star(\omega_0)$ and $m=1,\ldots,N_\omega$, where N_ω is the number of frequency subbands used to parametrize the bandwidth. De-

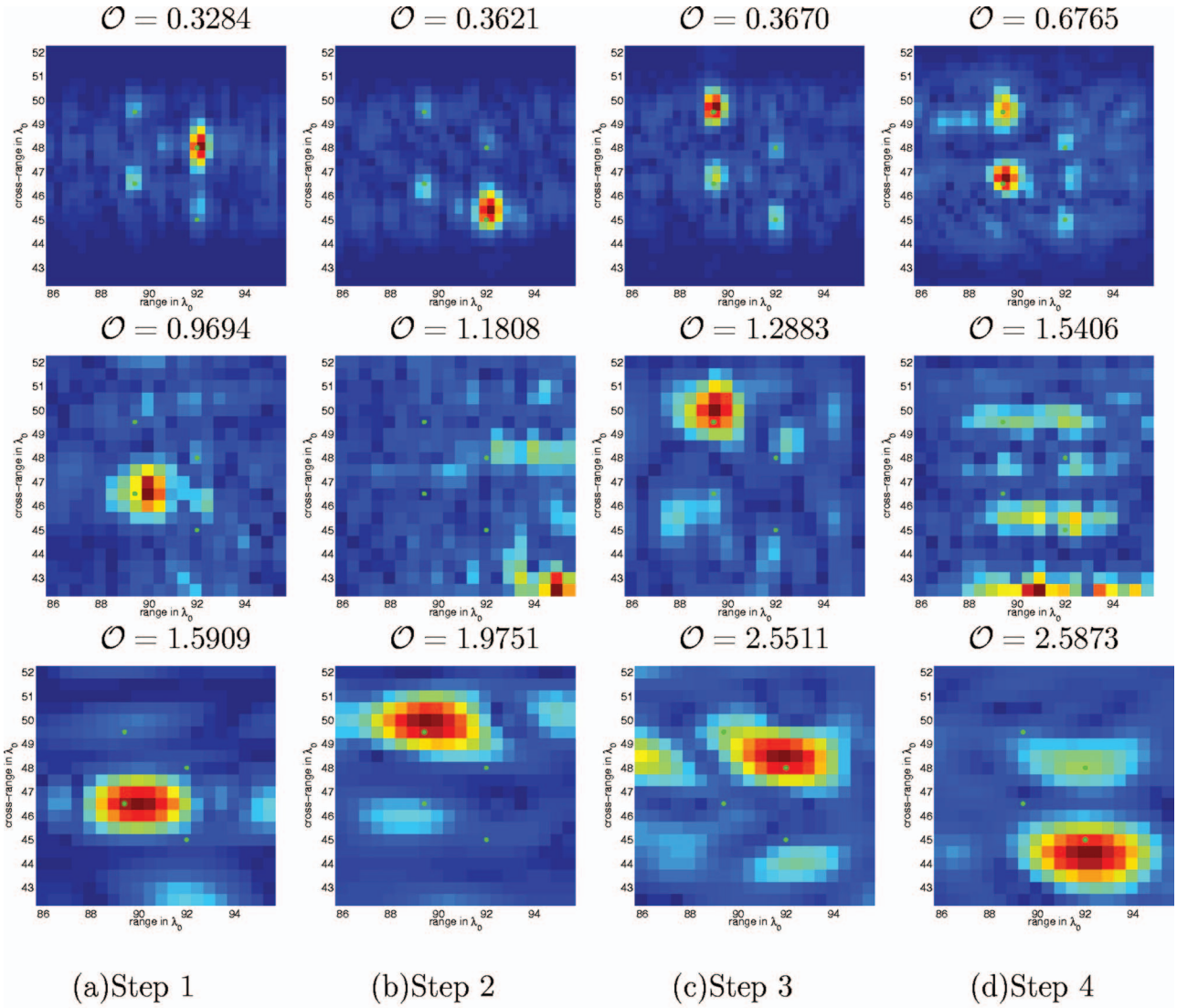

FIG. 6. Images with optimally selected $d_j(\omega)$ and uniform weights ω. Top row: homogeneous medium, middle row: Cluttered medium using $X_d = a$ and $\Omega_d = B$. Bottom row: Cluttered medium using X_d and Ω_d obtained by the adaptive algorithm. The scatterers are indicated with green dots in the image. Above each plot we give the value of the objective function $\mathcal{O}$.

note the resulting optimal filter by $D(\omega, d^{(1)})$.

Remark 1 *We show in the bottom left picture of Fig. 6 the image obtained with the optimal filter $D(\omega, d^{(1)})$, in the setup described in Sec.* II A. *The image is focused on a single scatterer and the optimally filtered data $D(\omega, d^{(1)})\hat{\Pi}(\omega)$ corresponds to the echoes from this scatterer alone. The optimal subspace weights $d^{(1)}$ are ploted in the bottom left picture of Fig. 7.*

Step 2: In order to image the next scatterer, we use filters that mask the scatterer found in Step 1, as follows. Let us denote by $J(\omega, 1)$ the index of the largest subspace weight

$$d^{(1)}_{J(\omega,1)}(\omega) = \max_{j=1,\ldots,n^\star(\omega_0)} d^{(1)}_j(\omega). \tag{24}$$

We define the map $\delta^{(1)}: [\omega_0 - \frac{B}{2}, \omega_0 + \frac{B}{2}] \to \mathbb{N}$ which takes a frequency ω in the bandwidth and returns

$$\delta^{(1)}(\omega) = \begin{cases} J(\omega, 1) & \text{if } d^{(1)}_{J(\omega,1)}(\omega) > 0, \\ 0 & \text{otherwise.} \end{cases} \tag{25}$$

Now we seek the optimal filter $D(\omega, d^{(2)})$ for $|\omega - \omega_0| \leqslant B/2$ by minimizing the objective function Eq. (23) over all the subspace weights in

$$\Delta^{(1)} = \{d_j(\omega) \in \Delta,\ d_j(\omega) = 0 \text{ if } j = \delta^{(1)}(\omega),$$
$$\text{for } |\omega - \omega_0| \leqslant \frac{B}{2},\ j = 1, \ldots, n^\star(\omega_0)\}.$$

Remark 2 *We show in Fig. 7 the optimal subspace weights $d^{(2)}$ and in Fig. 6 the images obtained with $D(\omega, d^{(2)})$. The objective function is larger than that at Step 1 because of the additional constraints in $\Delta^{(1)}$. The images are focused on a single scatterer, which is different from the one in Step 1. That scatterer has been masked by restricting the search to the set $\Delta^{(1)} \subset \Delta$.*

⋮

Step p: At the pth iteration we mask the scatterers found at Steps $1, \ldots, p-1$ and we seek the optimal filter $D(\omega, d^{(p)})$

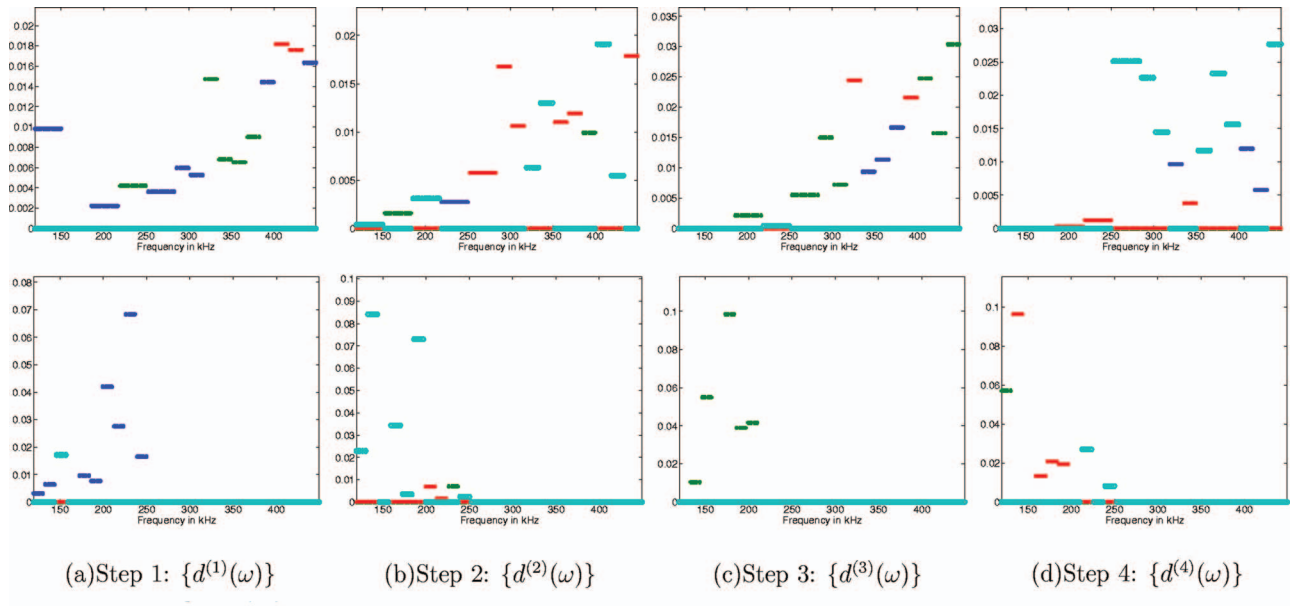

FIG. 7. Optimal $d_j^{(p)}(\omega)$, $j=1,\ldots,4$, $p=1,\ldots,4$. Top row: homogeneous medium. Bottom row: random medium. Only the largest coefficients in each frequency band are shown, and $d_1^{(p)}(\omega)$ are in blue, $d_2^{(p)}(\omega)$ in green, $d_3^{(p)}(\omega)$ in red and $d_4^{(p)}(\omega)$ in cyan (light blue). The pth column is for the p iteration, with $p=1,\ldots,4$.

that minimizes the objective function (23) over the subspace weights in

$$\Delta^{(p)} = \{d_j(\omega) \in \Delta^{(p-1)}, d_j(\omega) = 0 \ \text{ if } j = \delta^{(p-1)}(\omega),$$
$$\text{for } |\omega - \omega_0| \leqslant \frac{B}{2}, \ \ j = 1, \ldots, n^\star(\omega_0)\}.$$

⋮

The iteration terminates at the $n^\star(\omega_0)$ step, where we have used all the degrees of freedom in the array response matrix.

B. Optimal illumination algorithm

The images obtained with the selective imaging algorithm described in Sec. IV A can be improved further by assigning optimal weights to each source in the array, as we now describe. Let

$$\mathcal{W} = \left\{ w_s \geqslant 0 \text{ for } s = 1, \ldots, N; \ \sum_{s=1}^{N} w_s = 1 \right\}$$

be the set of weights that we can assign to the sources in the array and define for any $d \in \Delta$ and any weights in $\mathcal{W}$ the CINT imaging function

$$\mathcal{I}^{\text{CINT}}(\mathbf{y}^S;\Omega_d,\kappa_d;d,w) = \int_{|\omega-\omega_0|\leqslant\frac{B}{2}} d\omega \int_{\substack{|\omega'-\omega_0|\leqslant\frac{B}{2} \\ |\omega-\omega'|\leqslant\Omega_d}} d\omega' \times \sum_{r,r'\in\chi\left(\frac{\omega+\omega'}{2},\kappa_d\right)} \sum_{s,s'\in\chi\left(\frac{\omega+\omega'}{2},\kappa_d\right)} w_s \times \hat{Q}_d(\mathbf{x}_r,\mathbf{x}_s,\omega;\mathbf{y}^S) w_{s'} \overline{\hat{Q}_d(\mathbf{x}_{r'},\mathbf{x}_{s'},\omega';\mathbf{y}^S)}. \tag{26}$$

Here $\hat{Q}_d(\mathbf{x}_r,\mathbf{x}_s,\omega;\mathbf{y}^S)$ is the filtered data migrated to $\mathbf{y}^S$, and given by Eq. (12)

For a given data filter $D(\omega,d)$ with $|\omega-\omega_0| \leqslant B/2$, the optimal illumination w is the minimizer of the objective function

$$\mathcal{O}(\omega) = \|\mathcal{J}(\cdot;w)\|_{L^1(\mathcal{D})},$$

$$\mathcal{J}(\mathbf{y}^S;w) = \frac{|\mathcal{I}^{\text{CINT}}(\mathbf{y}^S;\Omega_d,\kappa_d;d,\omega)|^{1/2}}{\sup_{\mathbf{y}^S\in\mathcal{D}}|\mathcal{I}^{\text{CINT}}(\mathbf{y}^S;\Omega_d,\kappa_d;d,\omega)|^{1/2}} \tag{27}$$

over the set $\mathcal{W}$. This can be used in conjunction with the optimal selective illumination algorithm as follows.

The optimal illumination algorithm: For $p=1,\ldots,n^\star(\omega_0)$ determine the optimal filters $D(\omega,d^{(p)})$ for $|\omega-\omega_0| \leqslant B/2$ as described in Sec. IV A. Then compute for any given p the optimal illumination $w^{(p)}$, which minimizes over the set $\mathcal{W}$ the objective function (27) computed with $d=d^{(p)}$.

Remark 3 *We illustrate this algorithm with numerical simulations in the setup described in Sec.* II A. *The source weights are shown in Fig.* 9 *and the images are shown in Fig.* 8.

To explain how the algorithm works, let us consider the source at $\mathbf{x}_s$. Its contribution to the imaging function (26) is in the term

$$w_s[D(\omega,d)\hat{\Pi}(\omega)]_{r,s} \quad \text{for } r = 1, \ldots, N_s. \tag{28}$$

Suppose for simplicity that we have a single scatterer and $M=n^\star(\omega_0)=1$. Then Eq. (28) $d=d^{(1)}$ is just the sth column of the response matrix, corresponding to the illumination of the scatterer from the source at $\mathbf{x}_s$. The image with the source at $\mathbf{x}_s$ peaks naturally at the location of the scatterer. However, the focusing can be sharpened by using all the sources with optimal weights, as we have shown in Ref. 21.

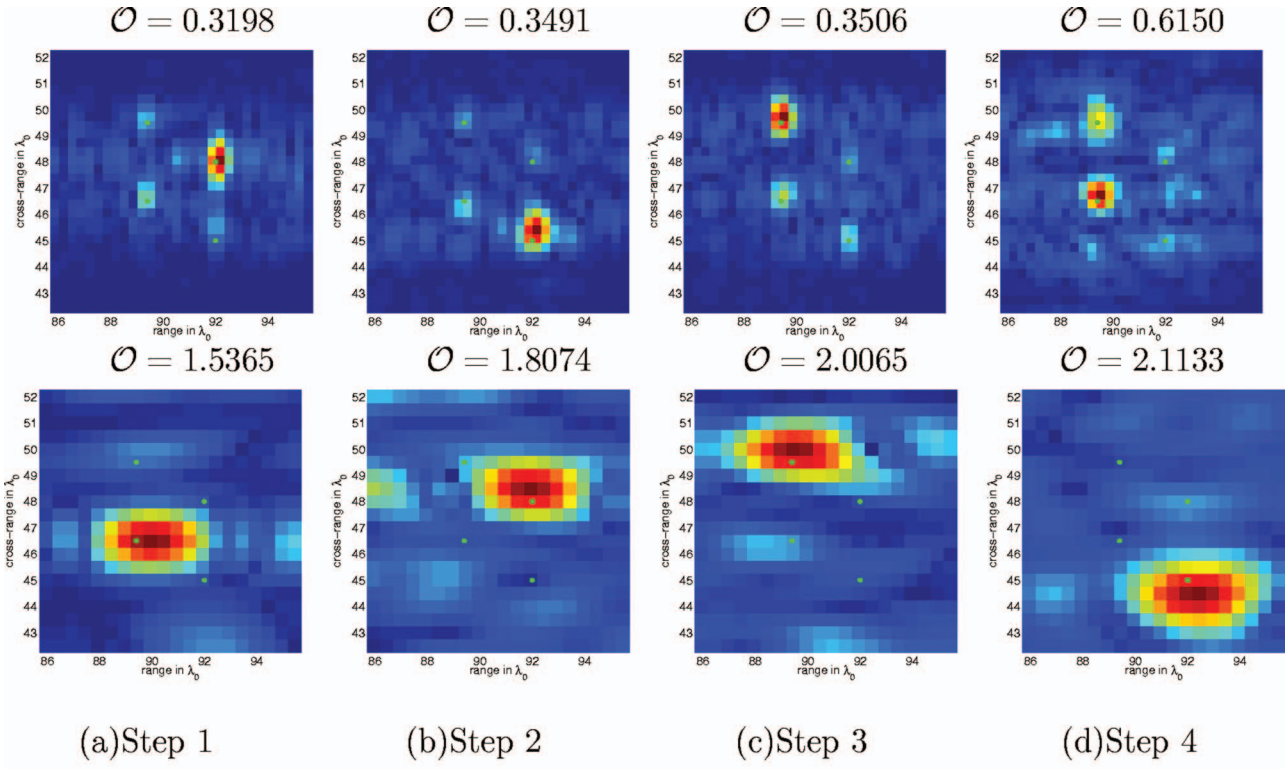

FIG. 8. Images with optimally selected $d_j(\omega)$ and weights ω. Top row: Homogeneous medium, bottom row: Cluttered medium using X_d and Ω_d obtained by the adaptive algorithm. The scatterers are indicated with green dots in the image. Above each plot we give the value of the objective function $\mathcal{O}$.

When we have a cluster of scatterers the algorithm works in a similar way. The selective imaging algorithm gives at step p an image that is focused on the pth scatterer. The filtered data $D(\omega, d^{(p)})\hat{\Pi}(\omega)$ correspond approximately to the echoes from this scatterer alone, and the image is sharpened by using the optimal illumination $w^{(p)}$ from the array.

V. NUMERICAL IMPLEMENTATION AND RESULTS

In the implementation of the algorithms, the search point $\mathbf{y}^S$ is in a square domain of size $10\lambda_0 \times 10\lambda_0$, centered at the center of mass of the scatterers. This domain is discretized using a uniform grid of 31×31 points and thus the discretization step is $\lambda_0/3$. It is in this domain that we present all the images in the paper (see Figs. 3, 5, 6, and 8).

Details regarding the implementation of the adaptive CINT algorithm can be found in Ref. 5. In order to save computational time when implementing the selective imaging algorithm, we divide the bandwidth B into 15 subbands. In the lower frequency range, for $\omega \in [150,300]$ kHz, we take 5 subbands of size 30 kHz while in the higher frequency range, for $\omega \in [300,450]$ kHz, we take a finer discretization

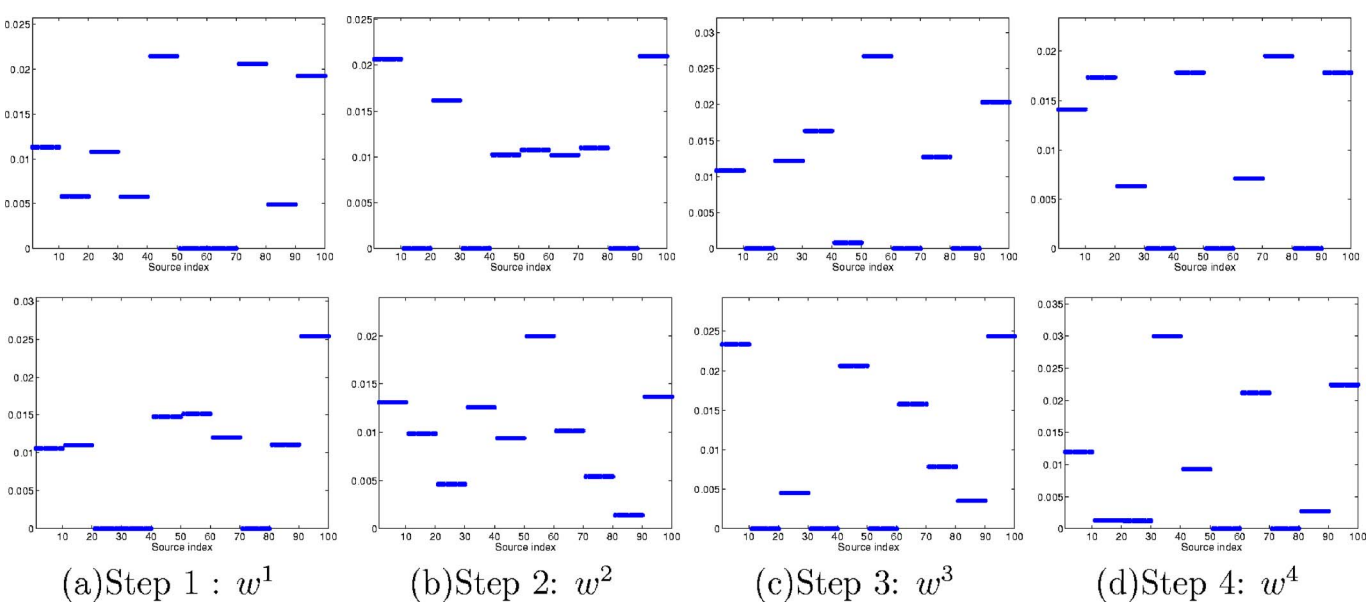

FIG. 9. (Color online) The optimal weights. Top row: homogeneous medium. Bottom row: cluttered medium.

using ten subbands of size 15 kHz. In each subband the subspace weights $d_j(\omega)$ are constant. This means that for the selective imaging algorithm we have 60 unknowns because we use $n^\star(\omega_0)=4$. In the cluttered medium, we tried first this discretization of the frequency and noted that the coefficients $d_j(\omega)$ are mostly zero for frequencies ω outside of [150,250] kHz. We therefore changed the discretization. In the cluttered medium we use nonzero $d_j(\omega)$ only in the lower part of the bandwidth, that is, for $\omega \in [150,250]$ kHz. The results shown in the bottom row of Fig. 7 are obtained by dividing this part of the bandwidth into ten subbands of size 10 kHz and taking the subspace weights $d_j(\omega)$ to be constant in each subband. The optimal coefficients $d_j(\omega)$ for homogeneous and random media are shown in Fig. 7. The convention for the colors in Fig. 7 is the following: we use the blue color for $d_1(\omega)$, green for $d_2(\omega)$, red for $d_3(\omega)$ and cyan for $d_4(\omega)$.

In the implementation of the optimal illumination algorithm, we group the array weights into blocks of ten elements and take the weights w to be constant in each block. The number of variables in this optimization problem is ten. The optimal weights for homogeneous and random media are shown in Fig. 9.

Because the scatterers are close to each other in our numerical simulations, we cannot image them separately with the DORT method as can be seen clearly in the top row of Fig. 5, which is in a homogeneous medium. There are more elaborate implementations of DORT that use continuation methods for singular values along frequencies. These may give better results in homogeneous media. However, DORT in its various implementations cannot be used in cluttered media, because it gives noisy and unstable images. In the images in the bottom row of Fig. 5, we note that as we go from left to right the results deteriorate. The last image in particular is just noise.

We see a big improvement in Fig. 6 bottom row, where the images are obtained with the selective subspace algorithm. We note that we image the scatterers one by one, both in the homogeneous and in the cluttered medium. The discretization of the bandwidth in the selective imaging process significantly affects the results. On one hand, coarser parametrizations lead to fewer optimization variables and lower computational cost. On the other hand, the image quality suffers from coarse parametrizations. This can be seen in the images in the top row of figure, which is for a homogeneous medium. They are better than the DORT images shown in the top row of Fig. 5, but we still see some ghosts. However, when we refine the bandwidth parametrization, the results improve.

By comparing the images in the middle and bottom rows of Fig. 6, we see that it is crucial to use a statistically stable method in clutter, such as CINT. When we do not have statistically stable results, the optimal subspace selection does not make sense. This is seen in the middle row of Fig. 6, where travel-time migration is used instead of CINT. The bottom row in Fig. 6 shows how selective imaging works in clutter. Here the resolution is naturally worse than that in the homogeneous case. This is expected because, as we explained Sec. III, with CINT we give up some resolution to gain stability in clutter.

The results are further improved with the optimal illumination algorithm, as shown in the images of Fig. 8. For both homogeneous and random media, the use of the optimal weights improves the quality of the images by reducing sidelobes. The improvement is more visible in cluttered media.

VI. SUMMARY AND CONCLUSIONS

We introduce a three-part algorithm for imaging small nearby scatterers in a randomly inhomogeneous medium. We assess its performance with numerical simulations in the context of ultrasonic array imaging of concrete structures. Travel-time migration is not effective and gives images that have speckles and are unstable because of significant multiple scattering from the inhomogeneities. Adaptive coherent interferometry (CINT) is effective in stabilizing the image at the expense of some blurring, which makes nearby scatterers difficult to identify. The algorithm presented in this paper uses adaptive CINT combined with (1) optimal subspace selection using the singular value decomposition (SVD) of the array response matrix, and (2) with optimal illumination. This algorithm is much more demanding computationally than travel-time migration, but it is quite effective for imaging in clutter.

ACKNOWLEDGMENTS

The work of L.B. was partially supported by the Office of Naval Research, under Grants No. N00014-05-1-0699 and by the National Science Foundation, Grant Nos. DMS-0604008, DMS-0305056, DMS-0354658. The work of G.P. was supported by Grants Nos. ONR N00014-02-1-0088, 02-SC-ARO-1067-MOD 1 and NSF DMS-0354674-001. The work of C.T. was partially supported by the Office of Naval Research, under Grant No. N00014-02-1-0088 and by 02-SC-ARO-1067-MOD 1.

[1]L. Borcea, G. Papanicolaou, and C. Tsogka, "Interferometric array imaging in clutter," Inverse Probl. **21**, 1419–1460 (2005).
[2]L. Borcea, G. Papanicolaou, and C. Tsogka, "Coherent interferometric imaging," Geophysics **71**, SI165–SI175 (2006).
[3]J. F. Claerbout and S. M. Doherty, "Downward continuation of moveout-corrected seismograms," Geophysics **37**, 741–768 (1972).
[4]N. Bleistein, J. Cohen, and J. W. Stockwell, *Mathematics of Multidimensional Seismic Imaging, Migration, and Inversion* (Springer, New York, 2001).
[5]L. Borcea, G. Papanicolaou, and C. Tsogka, "Adaptive interferometric imaging in clutter and optimal illumination," Inverse Probl. **22**, 1405–1436 (2006).
[6]L. Borcea, G. Papanicolaou, and C. Tsogka, "Asymptotics for the space-time Wigner transform with applications to imaging," in *Stochastic Differential Equations: Theory and Applications. Volume in Honor of Professor Boris L. Rozovskii*, edited by P. H. Baxendale and S. V. Lototsky, Vol. 2 of *Interdisciplinary Mathematical Sciences* (World Scientific, Singapore, 2007), pp. 91–112.
[7]C. Prada, J. L. Thomas, and M. Fink, "The iterative time-reversal process: Analysis of the convergence," J. Acoust. Soc. Am. **97**, 62–71 (1995).
[8]G. Montaldo, M. Tanter, and M. Fink, "Revisting iterative time reversal processing: Application to detection of multiple targets," J. Acoust. Soc. Am. **115**, 776–784 (2004).
[9]M. Cheney, D. Isaacson, and M. Lassas, "Optimal acoustic measurements," SIAM J. Appl. Math. **61**, 1628–1647 (2001).

[10]P. Blomgren, G. Papanicolaou, and H. Zhao, "Super-resolution in time-reversal acoustics," J. Acoust. Soc. Am. **111**, 238–248 (2002).
[11]G. Papanicolaou, L. Ryzhik, and K. Solna, "Self-averaging from lateral diversity in the Itô-Schrödinger equation," SIAM J. Multiscale Modeling and Simulation **6**, 468–492 (2007).
[12]C. Prada and M. Fink, "Eigenmodes of the time reversal operator: A solution to selective focusing in multiple-target media," Wave Motion **20**, 151–163 (1994).
[13]K. J. Langenberg, R. Marklein, K. Mayer, T. Krylov, P. Ampha, M. Krause, and D. Streicher, "Wavefield inversion in nondestructive testing," in *Electromagnetics in a Complex World—Challenges and Perspectives*, edited by I. M. Pinto, V. Galdi, and L. B. Felsen (Springer, New York, 2003), pp. 277–285.
[14]R. Marklein, K. J. Langenberg, K. Mayer, J. Miao, A. Shilivinski, A. Zimmer, W. Müller, V. Schmitz, C. Kohl, and U. Mletzko, "Recent applications and advances of numerical modeling and wavefield inversion in nondestructive testing," Adv. Radio Sci. **3**, 167–174 (2005).
[15]E. Bécache, P. Joly, and C. Tsogka, "An analysis of new mixed finite elements for the approximation of wave propagation problems," SIAM (Soc. Ind. Appl. Math.) J. Numer. Anal. **37**, 1053–1084 (2000).
[16]L. Ryzhik, G. Papanicolaou, and J. B. Keller, "Transport equations for elastic and other waves in random media," Wave Motion **24**, 327–370 (1996).
[17]M. C. W. van Rossum and T. M. Nieuwenhuizen, "Multiple scattering of classical waves: Microscopy, mesoscopy, and diffusion," Rev. Mod. Phys. **71**, 313–371 (1999).
[18]A. Derode, A. Tourin, and M. Fink, "Limits of time-reversal focusing through multiple scattering: Long range correlation," J. Acoust. Soc. Am. **107**, 2987–2998 (2000).
[19]M. Born and E. Wolf, *Principles of Optics* (Academic, New York, 1970).
[20]G. Christakos, *Random Field Models in Earth Sciences* (Dover, New York, 2005).
[21]L. Borcea, G. Papanicolaou, and C. Tsogka, "Optimal waveform design for array imaging," Inverse Probl. **23**, 1973–2020 (2007).
[22]E. Kerbrat, C. Prada, D. Cassereau, and M. Fink, "Imaging in the presence of grain noise using the decomposition of the time reversal operator," J. Acoust. Soc. Am. **113**, 1230–1240 (2003).
[23]J.-P. Fouque, J. Garnier, G. Papanicolaou, and K. Solna, "*Wave Propagation and Time Reversal in Randomly Layered Media* (Springer, New York, 2007).
[24]L. Borcea, G. Papanicolaou, C. Tsogka, and J. Berryman, "Imaging and time reversal in random media," Inverse Probl. **18**, 1247–1279 (2002).
[25]L. Borcea, G. Papanicolaou, C. Tsogka, and J. Berryman, "Statistically stable ultrasonic imaging in random media," J. Acoust. Soc. Am. **112**, 1509–1522 (2002).